

## Segmentation and Measurements of Major Blood Vessels from CT Pulmonary Angiography Using Deep Learning

Ali Teymur Kahraman<sup>1</sup>, Tomas Fröding<sup>2</sup>, Dimitris Toumpanakis<sup>3,4</sup>, Christian Jamtheim Gustafsson<sup>5,6\*</sup>, Tobias Sjöblom<sup>1\*†</sup>

<sup>1</sup>Ali Teymur Kahraman, MSc.

Department of Immunology, Genetics and Pathology, Uppsala University, Uppsala, Sweden.

<sup>2</sup> Tomas Fröding, MD, Radiologist.

Department of Radiology, Nyköping Hospital, Nyköping, Sweden.

<sup>3,4</sup> Dimitrios Toumpanakis, MD, Radiologist.

Consultant, Neuroradiology, Karolinska University Hospital, Stockholm, Sweden

PhD fellow, Department of Surgical Sciences, Uppsala University

<sup>5,6\*</sup>**Co-Senior Author:** Christian Jamtheim Gustafsson, Ph.D., Associate Professor, Medical Physicist.

Radiation Physics, Department of Hematology Oncology and Radiation Physics, Skåne University Hospital, Lund, Sweden

Department of Translational Sciences, Medical Radiation Physics, Lund University, Malmö, Sweden

<sup>1\*†</sup>**Corresponding and Co-Senior Author:** Tobias Sjöblom, Ph.D., Professor.

Department of Immunology, Genetics and Pathology, Uppsala University, Uppsala, Sweden

**Phone:** +46-18-4715036, **Cell:** +46-701-679039

**E-mail:** tobias.sjoblom@igp.uu.se

**Address:** Tobias Sjöblom, Ph. D., Professor, Department of Immunology, Genetics and Pathology, Uppsala University, Rudbeck Laboratory SE-751 85 Uppsala, Sweden

### **Co-Senior author contributions**

Christian Jamtheim Gustafsson and Tobias Sjöblom are listed as co-senior authors for their equal contributions to the project's supervision.

## **Abstract**

### **Background**

Measuring major blood vessels from CT pulmonary angiography examinations (CTPAs) to assess cardiovascular diseases has the potential to improve overall patient outcomes. However, this process is time-consuming and prone to errors. Deep learning (DL) approaches offer the potential to enhance accuracy, speed, and consistency.

### **Objectives**

To develop and train a deep learning-based algorithm capable of automatically and accurately segmenting and measuring major blood vessels in CTPAs.

### **Methods**

Seven hundred CTPAs from 652 patients were retrospectively collected at a single center. The dataset was split into two subsets, one for training and cross-validation ( $n = 490$ ) and one for assessing model performance ( $n = 210$ ). The segmentation masks for the descending aorta (DAo), ascending aorta (AAo), and pulmonary trunk (PT) were generated by our previously developed segmentation model and were quantitatively validated by two radiologists. These validated masks were subsequently used as ground truth for model training. An U-Net deep learning model was created using the nnU-Net framework and trained on 490 CTPAs with 5-fold cross-validation. Following the training, the model was applied to volumes of interest in the images to generate a pool of candidate regions containing potential vessels. A vessel detection algorithm was developed and used on the candidate pool to identify vessels followed by measurement. The final model was evaluated on 210 and 47 CTPAs from internal and external datasets, respectively.

### **Results**

Assessing model segmentation performance on the internal evaluation set, the median Dice scores were 0.95 for the DAo, 0.96 for the AAo, and 0.95 for the PT. The model measurements showed a strong correlation with those made by the radiologist, with Pearson's  $r$  values of 0.91 for image noise, 0.98 for intravenous contrast concentration in the PT, 0.93 for AAo diameter,

and 0.55 for PT diameter ( $P < .001$ ). Additionally, the AAo segmentation (median Dice score 0.94) and the PT diameter measurement ( $r = 0.77$ ) were evaluated in two external datasets.

## **Conclusions**

The fully automated, deep learning-based algorithm accurately segmented and measured major blood vessels in real-world CTPAs.

## **Keywords**

Computer-aided detection, computed tomography pulmonary angiography, deep learning, nnU-Net, pulmonary embolism, pulmonary hypertension.

## **Abbreviations**

AAo = ascending aorta

CADe = computer-aided detection.

CTPA = computed tomography pulmonary angiography

DAo = descending aorta

HU = Hounsfield unit

DL = deep learning

IV = intravenous

nnU-Net = no-new-U-Net

PE = pulmonary embolism

PT = pulmonary trunk

## **Main Text**

### **Introduction**

Cardiovascular disease (CVD) is the leading cause of morbidity and mortality worldwide [1]. Identification and accurate measurement of major blood vessels within the thoracic cavity is essential for radiologists in the diagnosis and assessment of CVDs [2–4]. Computed tomography (CT) pulmonary angiography (CTPA) is the gold standard for diagnosing pulmonary embolism (PE) and involves the use of an intravenous (IV) contrast agent to enhance the visualization of pulmonary arteries [5,6]. Additionally, CTPA enhances the visibility of other major blood vessels in the chest cavity, enabling radiologists to assess CVDs more effectively [7,8]. Several CVDs, such as chronic thromboembolic pulmonary hypertension (CTEPH), pulmonary arterial hypertension (PAH), and aortic aneurysms, can be diagnosed or suspected based on the presence of enlarged pulmonary arteries or an enlarged ascending aorta [9–11]. Therefore, a fully automated solution has the potential to improve radiologists' workflow efficiency and accuracy and enhance overall patient outcomes.

Existing automatic methods for segmenting and measuring major blood vessels in the chest cavity often rely on traditional image processing and analysis techniques [12–14]. While deep learning-based solutions have shown promise [15–17], many existing datasets have limitations, including small sample sizes and a lack of representative artifacts and co-morbidities. To address these challenges, we propose training and testing the state-of-the-art semantic segmentation deep learning framework, the no-new-U-Net (nnU-Net) [18], on a large and diverse dataset of CTPA examinations. This dataset is designed to accurately reflect the range of imaging conditions encountered in clinical practice [19]. The nnU-Net framework represents a significant advancement in U-Net model training, automating the process of hyperparameter optimization and model selection [18]. In this study, we developed a deep learning model utilizing the nnU-Net architecture to automate the segmentation and measurement of major blood vessels within the thoracic cavity, specifically the descending aorta (DAo), ascending aorta (AAo), and pulmonary trunk (PT), in routine clinical contrast-enhanced CTPAs.

## **Materials and Methods**

### **Internal dataset**

We retrospectively collected a dataset of 700 non-ECG-gated CTPA examinations performed between 2014 and 2018 at a single institution (Nyköping Hospital, Sweden), with approval from the Swedish Ethical Review Authority (EPN Uppsala Dnr 2015/023 and 2015/023/1) for the collection and analysis of CTPA examinations [19]. The CTPAs were routine clinical examinations, exported sequentially from the history list in the institution's Picture Archiving and Communication System (PACS) in Digital Imaging and Communications in Medicine (DICOM) format, with all personal identifiers removed from the headers using the Dicom2USB hardware solution ([www.dicom2usb.com](http://www.dicom2usb.com)).

### **CT Acquisition Protocols**

Five CT scanners were used to acquire the CTPAs: Brilliance 64, Ingenuity Core, and Ingenuity CT (Philips, Netherlands); LightSpeed VCT (GE Healthcare, USA); and Somatom Definition Flash (Siemens, Germany). Scans were performed using a bolus tracking method with the region of interest in the pulmonary trunk, utilizing pixel spacing of 0.59–0.98 mm, tube voltages of 80–120 kV, and slice thicknesses of 0.625–2.0 mm. The contrast medium (Omnipaque 350 mg I/ml, GE Healthcare) was administered in doses ranging from 20 to 114 ml (mean 62 ml) at injection rates of 2.4 to 6.1 ml/s (mean 3.6 ml/s). Secondary reconstructions with a 2.0 mm slice thickness were applied to all examinations in the internal dataset. All annotations and measurements were performed in the axial plane, providing standardized data for model development and inference.

### **Data annotation**

In previous work, we developed a fully automated deterministic algorithm for segmenting and measuring major vessels in CTPA examinations [19]. In this study, we utilized the previously developed deterministic solution to generate 2D segmentation masks, which serve as the ground truth for the major blood vessels in the thoracic cavity: the descending aorta (DAo), ascending aorta (AAo), and pulmonary trunk (PT). These ground truth segmentation masks were validated by two radiologists, DT and TF, with 7 and 17 years of experience in chest radiology, respectively. A single 2D segmentation mask for each vessel was obtained from each CTPA volume at a specific anatomical location, either at the carina of the trachea or the level of the pulmonary trunk. This automated process successfully generated 2D segmentation masks for

major blood vessels in 596 out of 700 CTPAs, with validation by the radiologists, resulting in a total of 1,788 validated masks. However, the remaining 104 CTPAs required manual annotation, as they could not be processed automatically. This manual annotation produced an additional 312 2D segmentation masks for the three major blood vessels, using the open-source software Medical Imaging Interaction Toolkit (MITK) [20]. The manual annotations for these 104 CTPAs were also validated by DT and TF to ensure consistency and accuracy. The manual (DT and TF) ground truth measurements of major blood vessels included the diameter of the AAo and the PT, the IV contrast concentration in the PT (mean HU value in 2 cm<sup>2</sup> ROI) and the image noise (standard deviation of HU in 1 cm<sup>2</sup> ROI in the DAo), as reported [19].

### **Examination quality of CTPA volume images**

The examination quality metrics and methodologies applied were developed and validated in [19], where a comprehensive analysis was conducted on the CTPA images to establish robust quality scoring criteria. In short, for each CTPA examination the radiologist assessed five image quality parameters that affect the evaluation for PE: motion artifacts, streak artifacts, IV contrast concentration in the PT, parenchymal disease and image noise. Each parameter was scored, resulting in classification of the quality of the CTPA as good, acceptable or inferior. For detailed information on the original formulation and calculation of the quality scores, please refer to the supplementary information of [19].

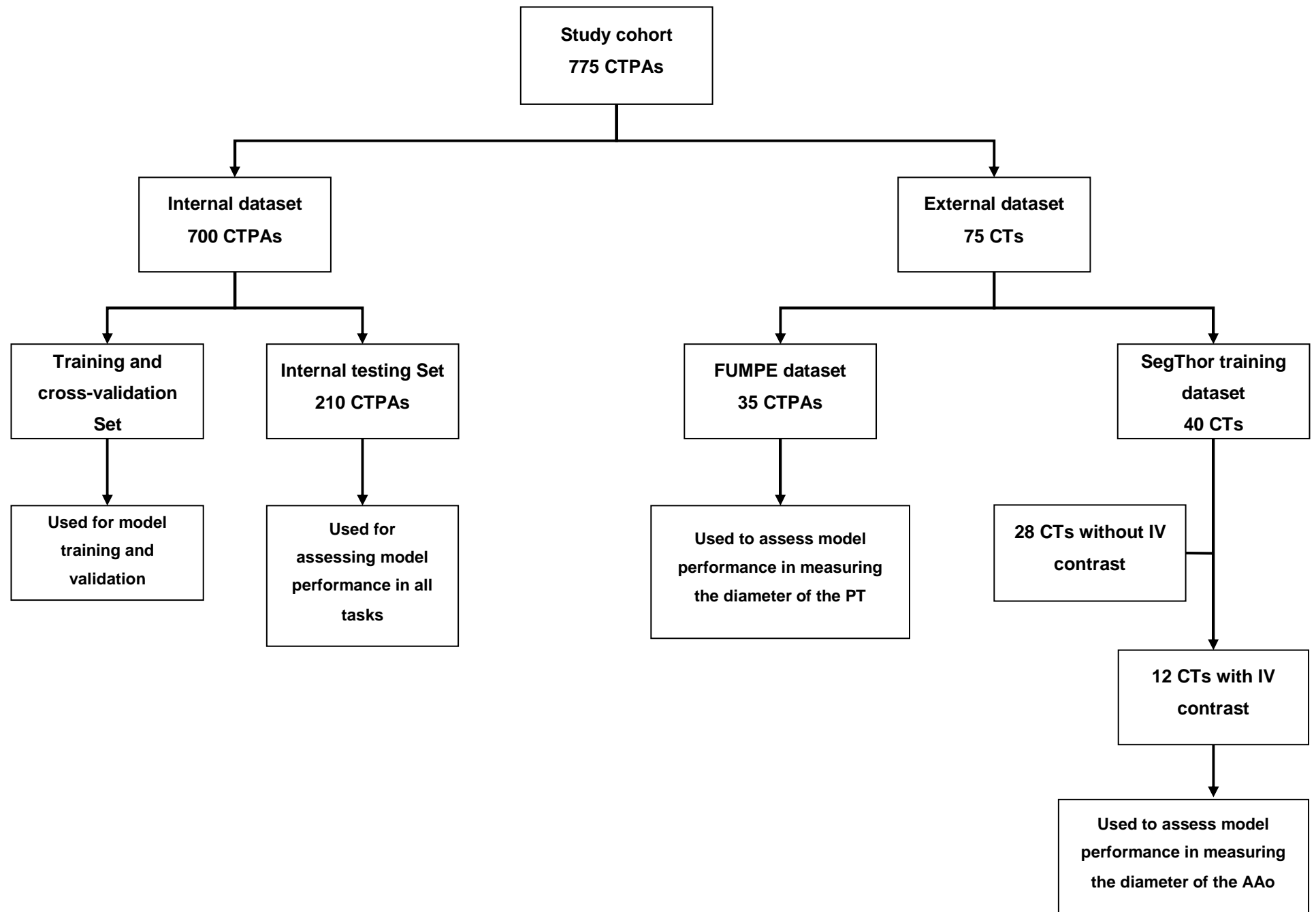


**Figure 1 Schematic of the study cohort.** From the internal dataset, 210 CT pulmonary angiography (CTPA) examinations were used for model testing across all tasks: measurement of image noise, intravenous (IV) contrast in the pulmonary trunk (PT), diameter of the ascending aorta (AAo), and diameter of the PT. The FUMPE dataset was used for external validation of PT diameter measurements. From the SegThor dataset, 28 CT examinations without IV contrast were excluded. The remaining 12 CT scans with IV contrast were used to test the diameter of the AAo.



## **External datasets**

Two publicly available datasets were used to externally evaluate the proposed algorithm: the Segmentation of Thoracic Organs at Risk in CT images (SegTHOR) [21] and the Ferdowsi University of Mashhad's PE dataset (FUMPE) [22]. The SegTHOR training set contains 40 CT scans with and without IV contrast, all with manual segmentation of the aorta. For the external evaluation of ascending aorta segmentation, 12 CT scans with IV contrast were selected from the 40 CT scans, while the remaining 28 CTs without IV contrast were excluded. The FUMPE dataset contains 35 CTPAs with the diameter of the pulmonary trunk (PT) annotated by radiologists, which were used for the external evaluation. An overview of our internal and external datasets is shown in **Figure 1**.

## **Computational Environment**

The computational environment used for both model training and inference on test data in this study includes specific software versions: Ubuntu (22.04.3 LTS) as the operating system, Docker (27.0.3) for containerization, and CUDA (12.1.1), along with Nvidia driver (535.183.01), to ensure seamless interaction with NVIDIA GeForce RTX 2080 Ti GPUs. The programming languages used are Python (3.10.6) and MATLAB R2023b (The MathWorks, Inc., Natick, Massachusetts, USA). The deep learning framework PyTorch (version 2.1.0) was utilized, and the nnU-Net framework was implemented in version 2.1.1. Post-processing computations were conducted on the same machine equipped with an Intel Core i9-9900X CPU (10 cores, 20 threads, 3.5 GHz base clock, 4.5 GHz boost clock).

## **Model training and validation**

For model training, the nnU-Net framework was implemented using the PyTorch Nvidia container (nvcr.io/nvidia/pytorch:24.04-py3) on a Docker platform (Docker Inc., Palo Alto, California, USA), providing an optimized environment for deep learning and scientific computing. The nnU-Net deep learning open-source framework is an adaptable and automated solution designed for semantic segmentation tasks, particularly in the field of medical image segmentation. It builds on a U-Net-like architecture with a contracting path (encoder) and an expansive path (decoder) with skip connections to efficiently capture and process image details. The framework automates the processes of data preprocessing, training pipeline, and network

configuration, including aspects such as network topology, depth, learning rate, filter selection, patch and batch size, based on the dataset characteristics, thereby eliminating the need for manual fine-tuning [18].

A 2D U-Net architecture with a depth of 7 was generated by the nnU-Net framework, designed for an initial input size of 512x512 pixels (Figure 2). In the downsampling operations (contracting path), each level consisted of a 2D convolutional layer with a kernel size of 3×3 and a stride of 2, followed by another 2D convolutional layer with the same kernel size but a stride of 1. The network started with 32 filters and increased up to 512 filters as the depth increases. In the upsampling operations (expansive path), a 2D transposed convolutional layer with a kernel size of 2×2 and a stride of 2 was used. Both downsampling and upsampling operations were followed by instance normalization and a leaky rectified linear unit (Leaky ReLU) activation.

During training, the nnU-Net framework utilized a tailored set of hyperparameters to optimize the learning process. The optimizer selected was Stochastic Gradient Descent (SGD) with Nesterov momentum, with a momentum value of 0.99. Weight decay was applied with a coefficient of 3e-05 to control model complexity. The training process was set to run for a maximum of 1000 epochs. To further refine the training, a learning rate scheduler was used, which progressively reduced the learning rate each epoch, starting at 0.01 and decreasing to 2e-05 by the final epoch. The nnU-Net framework employs a variety of data augmentation techniques to enhance model generalization and prevent overfitting to the training dataset. These techniques include spatial transformations such as rotations, scaling, and mirroring. Specifically, the rotations cover a full 360-degree range around the X-axis, with scaling applied between 0.7 to 1.4 times the original size. Mirroring is applied along both the X and Y axes. Additionally, Gaussian noise and blur, as well as brightness, contrast, and gamma transformations, are utilized to further augment the data and improve model robustness.

### **Model inference and post-processing**

After model training, three trained models were obtained for the segmentation tasks of the DAo, AAo, and PT. Before applying model inference, the volume of interest (VOI) was first determined by including only the slices between approximately 22% and 65% of the total size of

the CTPA volume. This approach ensured that most of the mediastinum was accurately captured, encompassing two key anatomical landmarks: the carina of the trachea and the level of the pulmonary trunk. Model inference was then applied only to this volume of interest to generate candidate pools for DAo, AAo, and PT segmentations. Once the candidates were obtained, deterministic algorithms were developed in MATLAB to identify the best 2D segmentation masks for measurement. The study design is illustrated in **Figure 2**.

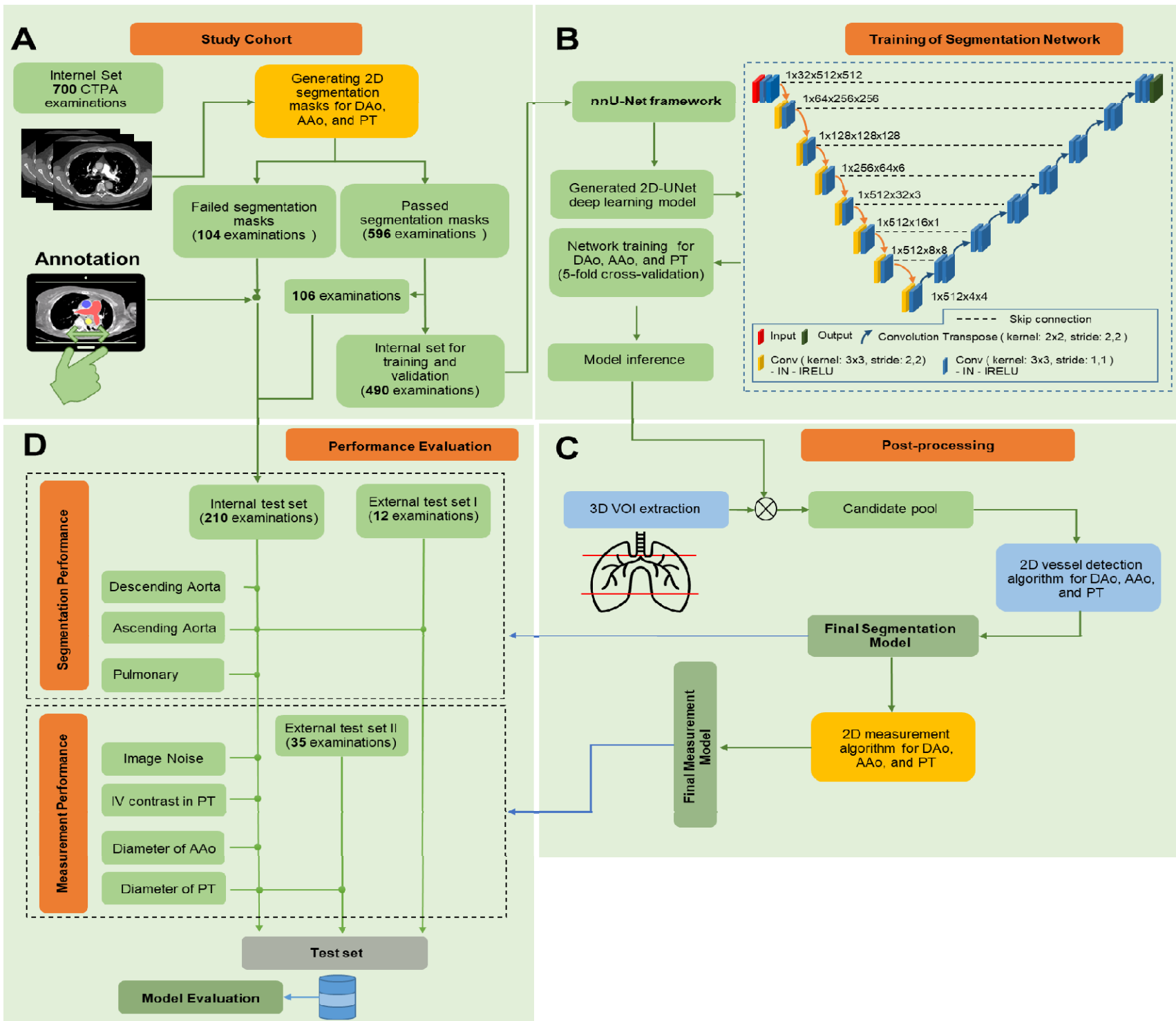


**Figure 2 Study Design.** 700 CT pulmonary angiography (CTPA) examinations were collected, and a fully automated deterministic segmentation algorithm [19] was applied to generate 2D segmentation masks for the descending aorta (DAo), ascending aorta (AAo), and pulmonary trunk (PT). Segmentation masks were successfully generated for 596 of these examinations, while the remaining 104 required manual annotation. The dataset was divided into a training set comprising 490 examinations and a testing set comprising 210 examinations (a). The 2D U-Net deep learning model, generated by the nnU-Net framework, was trained on 490 CTPA scans using 5-fold cross-validation. By default, the convolution layer used a  $3 \times 3$  filter size, followed by an instance normalization (IN) layer and a leaky rectified linear unit (lReLU) layer (b). Model inference was applied to the volume of interest (VOI) to generate a pool of vessel candidates. A 2D vessel detection algorithm was then applied to the candidate pool to determine the objects of interest for measurement. A 2D measurement algorithm [19] was subsequently applied to achieve accurate vessel measurements (c). For segmentation and measurement performance, the final model was evaluated on 210 CTPAs from the internal dataset and on 12 and 35 CTPAs from two publicly available datasets, respectively (d). Modules in gold-colored boxes represent previously developed solutions, while those in light blue-colored boxes were developed as part of this work.

### **Descending aorta segmentation**

To ensure the correct selection of the descending aorta (DAo) from the segmentation candidates, we first applied 3D connected component analysis to identify the largest component within the volume of interest (VOI), assuming it to be the DAo. Next, we removed any connected components with fewer than 200 pixels using 8-connectivity and performed a morphological closing operation on the binary image with a disk-shaped structuring element having a radius of 9 pixels. These image processing steps focused on isolating and refining the largest 3D structure, presumably the DAo, by filtering out smaller components and smoothing the object boundaries. Once we obtained the 3D segmentation of the DAo, we applied the same measurement algorithm used by radiologists. Specifically, the standard deviation of HU within a  $1 \text{ cm}^2$  circular region of interest (ROI) in the DAo was used as a measure of image noise in the CTPA examination. We calculated the image noise in every 2D segment of the 3D DAo segmentation and then took the median of these values. The median value of the image noise provided the final measurement.

### **Ascending Aorta Segmentation**

We began by applying a filtering operation to eliminate small, irrelevant objects from the candidate pool using an area opening operation, which removes connected components with fewer than 200 pixels based on 8-connectivity. Next, we performed a 3D connected component analysis, retaining only components with an area greater than 12,500 pixels. To ensure the spatial relevance of the selected component, likely representing the AAo, we calculated the z-coordinate

of the centroids of the filtered components. The component whose centroid was closest to the superior part of the CTPA was identified and retained for further processing. We then tracked any sudden area loss or significant shifts in centroid position to remove adjacent objects or irrelevant tissues. After these operations, a final connected component analysis using 26-connectivity was performed to select the largest remaining component in the candidate pool. Finally, a morphological closing operation with a disk-shaped structuring element with a radius of 9 pixels was applied to smooth the boundaries of the final 3D component. To measure the diameter of the AAo, we used the equivalent diameter property of the 'regionprops' function in MATLAB's image processing toolbox. We calculated the equivalent diameter for all 2D objects within the final 3D component, and the median value of these 2D equivalent diameters provided the final measurement.

### **Pulmonary Trunk (PT) Segmentation and IV contrast in PT**

We first eliminated components smaller than 200 pixels from the candidate pool. The candidate pool was further refined by applying morphological opening using a disk-shaped structuring element with a radius of 7 pixels, helping to remove noise and small irrelevant structures. Next, components with less than 10,000 pixels were removed, ensuring that only significant regions remain. To identify the components most likely corresponding to the pulmonary trunk within the candidate pool based on the slice number of the CTPAs, we established two reference points as follows:

Let  $S$  represent the total number of slices in the CTPA. Then:

$$\textit{Reference Point 1} = \textit{round} \left( \frac{S}{2} \right) - \textit{round} \left( \frac{S}{10} \right)$$

$$\textit{Reference Point 2} = \textit{round} \left( \frac{S}{2} \right) - \textit{round} \left( \frac{S}{16} \right)$$

The algorithm then calculates the distance of each component's centroid from the reference points and counts the number of slices above, below, and within the reference regions. If exactly

two components are present, the algorithm evaluates their proximity to the reference points and, based on the patient's position, selects the component that is either the highest or lowest in the scan volume as the pulmonary trunk. For three components, the algorithm prioritizes them according to their proximity to the reference points and selects the most appropriate one based on the patient's position. If more than three components are identified, the algorithm refines its selection criteria further, focusing on the second or third closest component, depending on the patient's position, to accurately identify the pulmonary trunk. Finally, the selected component undergoes a closing operation using a disk-shaped structuring element with a radius of 9 pixels to smooth the boundaries and complete the segmentation of the pulmonary trunk. As a measure of the IV contrast concentration in the PT, we calculated the mean HU of all 2D objects within the final 3D component. To measure the diameter of the PT, we extracted horizontal line segments based on the Hough transform for each 2D object within the final 3D component, and the median value of these 2D Hough lines provided the final diameter measurement.

## Statistical Analysis

The model's segmentation performance was evaluated using the Boundary F1 (BF) score, the Dice-Sørensen coefficient (DSC), and the Jaccard Index (JI) with Matlab (MathWorks, Inc., R2023b). The BF score evaluates the accuracy of the model segmentation boundary of an object by comparing it to the ground truth segmentation boundary [23]. The BF score is calculated as the harmonic mean of recall and precision:

$$BF = 2 * \frac{Recall * Precision}{(Recall + Precision)}$$

Here, *Recall* is the ratio of ground truth boundary points near the model segmentation boundary to the total ground truth segmentation boundary length. *Precision* is the ratio of model boundary points near the ground truth segmentation boundary to the total model segmentation boundary length.

Given two sets, A (model segmentation) and B (ground truth segmentation),

DSC is defined as:

$$DSC(A, B) = 2 * \frac{|A \cap B|}{|A| + |B|}$$

And JI defined as follow:

$$JI(A, B) = \frac{DSC(A, B)}{2 - DSC(A, B)}$$

Bland-Altman [24] and scatter plot analyses were used to evaluate measurement performance of the model. Specifically, Bland-Altman analysis assessed the agreement between the model's and the radiologist's measurements, while the scatter plot analysis examined the relationship between them. Pearson's correlation coefficient was utilized to evaluate the correlation between the model's and the radiologist's measurements. Subgroup analysis of radiologist measurements, based on examination quality, sex, and age, was conducted using the Kruskal-Wallis H-test. A p-value of less than 0.05 was considered statistically significant. For statistical analysis, we utilized SciPy, a Python library for scientific computing (version 1.13.1), and Microsoft Excel from Microsoft 365 (Microsoft Corporation, Washington, USA).



## Results

The internal dataset (n=700 CTPAs) included 383 CTPA examinations from 353 women (median age, 73 years; IQR, 20 years) and 317 examinations from 299 men (median age, 71 years; IQR 15 years) (**Table 1**). The internal dataset was split into training and testing sets using a 70/30 split ratio. For the training and 5-fold cross-validation sets, 1,470 2D segmentation masks from 490 CTPAs were selected. The remaining 630 2D segmentation masks from 210 CTPAs were used for the testing set. Additionally, all 312 manually annotated 2D segmentation masks from 104 CTPAs were included in the testing set. There is no patient overlap between the training and testing sets. For model training, each of the three major blood vessels (DAo, AAo, and PT) was trained separately using the internal dataset comprising 1,470 2D masks (490 masks per vessel) derived from 490 CTPAs. The segmentation models were trained using 5-fold cross-validation, with 80% of the data (a total of 1,176 2D masks, 392 masks per vessel) used for training and 20% (a total of 294 2D masks, 98 masks per vessel) used for cross-validation.

**Table 1 Study Characteristics of the Internal Dataset**

Characteristics	Training Dataset	Test Dataset	Overall
No. of patients	466	186	652
No. of CTPA exams	490	210	700
Sex (Women/Men)	245/221	108/78	353/299
Median age (IQR) years	72.0 (17.0)	74.0 (19.75)	72.0 (18.0)
Women	73.0 (19.0)	74.0 (22.5)	73.0 (20.0)
Men	71.0 (16.0)	74.0 (16.0)	71.0 (15.0)
Diseases			
Emboli in (Right/Left) lung	100/81	37/33	137/114
Pneumothorax in (Right/Left) lung	4/2	0/0	4/2
Pleural effusion in (Right/Left) lung	147/140	83/74	230/214
Infiltrate or atelectasis (or other opacities) in (Right/Left) lung	298/275	146/138	444/413
Pericardial fluid (excessive amounts)	57	26	83
Sign of acute congestive heart failure	89	42	131
Lymph nodes (Mediastinum/Right hilum/Left hilum) <sup>1</sup>	90/48/37	48/28/17	138/76/54
Quality of CTPA exams (Good/Acceptable/Inferior)	200/158/132	58/70/82	258/228/214

Note. — Unless otherwise indicated, data are number of examinations. CTPA = computed tomography pulmonary angiography

<sup>1</sup> Lymph nodes larger than 1 cm (short axis)

## **Radiologists Ground Truth Measurements**

The median image noise was 20.5 HU (IQR, 8 HU) in the internal training dataset and 20 HU (IQR, 10 HU) in the internal test dataset, with significant differences observed based on examination quality, sex, and age groups older than 64 years (**Table 2 and Supp. Table 1**). The median diameter of the AAo was 33 mm (IQR, 6 mm) in the internal training dataset and 34 mm (IQR, 6 mm) in the internal test dataset, with significant differences particularly noted across sex and older age groups. The median IV contrast concentration in PT was 394 HU (IQR, 146 HU) in the internal training dataset and 358 HU (IQR, 158 HU) in the internal test dataset, with significant differences observed in older patients, especially those aged over 79 years. The median diameter of the PT was 26 mm (IQR, 5 mm) in the internal training dataset and 28 mm (IQR, 6 mm) in the internal test dataset, without significant differences across examination quality, sex, or age groups.

**Table 2 Radiologists Ground Truth Measurements**

Category	Training Dataset (n=490)					Test Dataset (n=210)				
	Quality of CTPA exams				Overall	Quality of CTPA exams				Overall
	Good	Acceptable	Inferior	p-value		Good	Acceptable	Inferior	p-value	
No. of CTPA exams <sup>1</sup>										
Women	121 (24.69)	80 (16.33)	56 (11.43)		257 (52.45)	41 (19.52)	41 (19.52)	44 (20.95)		126 (59.99)
Men	79 (16.12)	78 (15.92)	76 (15.51)		233 (47.55)	17 (8.1)	29 (13.81)	38 (18.1)		84 (40.01)
Age < 65 years	62 (12.65)	50 (10.2)	33 (6.73)	-	145 (29.58)	16 (7.62)	21 (10)	23 (10.95)	-	60 (28.57)
Age 65-79 years	92 (18.78)	78 (15.92)	61 (12.45)		231 (47.15)	25 (11.9)	31 (14.76)	30 (14.29)		86 (40.95)
Age ≥ 80 years	46 (9.39)	30 (6.12)	38 (7.76)		114 (23.27)	17 (8.1)	18 (8.57)	29 (13.81)		64 (30.48)
Image noise (HU) <sup>2</sup>										
Overall	19.0 (9.0)	20.0 (7.0)	23.0 (7.0)	< 0.0001	20.5 (8.0)	16.0 (9.8)	20.0 (8.8)	23.5 (8.0)	< 0.0001	20.0 (10.0)
Women	19.0 (10.0)	20.5 (7.0)	21.0 (8.0)	0.02	20.0 (9.0)	16.0 (9.0)	20.0 (7.0)	23.0 (8.0)	0.0004	20.0 (10.0)
Men	20.0 (7.0)	20.0 (7.0)	23.5 (5.2)	0.0002	21.0 (8.0)	16.0 (9.0)	19.0 (10.0)	24.0 (8.8)	0.003	21.0 (9.5)
Age < 65 years	21.0 (8.0)	19.0 (7.8)	21.0 (8.0)	0.92	20.0 (8.0)	15.5 (12.2)	18.0 (8.0)	22.0 (6.5)	0.11	20.0 (9.5)
Age 65-79 years	18.5 (9.2)	20.5 (7.8)	23.0 (6.0)	0.0001	20.0 (9.0)	18.0 (7.0)	20.0 (8.0)	24.0 (7.8)	0.006	20.0 (8.8)
Age ≥ 80 years	19.0 (9.8)	20.5 (6.5)	23.5 (4.8)	0.001	21.0 (7.8)	14.0 (5.0)	21.0 (9.5)	24.0 (9.0)	0.0005	20.0 (10.8)
Diameter of ascending aorta (mm) <sup>3</sup>										
Overall	32.0 (6.0)	33.0 (5.0)	34.0 (6.0)	0.01	33.0 (6.0)	35.0 (6.5)	33.0 (6.0)	34.0 (6.0)	0.07	34.0 (6.0)
Women	31.0 (5.0)	32.0 (5.0)	32.0 (7.0)	0.45	31.0 (6.0)	34.0 (6.0)	31.0 (7.0)	32.0 (4.0)	0.11	33.0 (6.5)
Men	34.0 (6.0)	35.0 (4.8)	35.0 (5.2)	0.22	35.0 (5.0)	38.0 (7.0)	35.0 (4.0)	36.0 (4.8)	0.07	36.0 (5.0)
Age < 65 years	29.5 (6.0)	31.0 (5.8)	31.0 (8.0)	0.3	31.0 (7.0)	32.0 (7.8)	29.0 (6.0)	31.0 (5.0)	0.39	31.0 (7.0)
Age 65-79 years	34.0 (5.2)	34.0 (4.0)	34.0 (4.0)	0.72	34.0 (5.0)	35.0 (7.0)	33.0 (6.5)	35.0 (4.0)	0.28	35.0 (6.0)
Age ≥ 80 years	33.0 (6.0)	35.0 (5.8)	36.0 (5.8)	0.01	35.0 (7.0)	37.0 (3.0)	35.5 (3.5)	36.0 (6.0)	0.34	36.0 (5.0)
IV contrast concentration in PT (HU) <sup>□</sup>										
Overall	425 (125)	370 (134)	374 (193)	< 0.0001	394 (146)	406 (141)	334 (148)	316 (167)	< 0.0001	358 (158)
Women	432 (123)	363 (135)	351 (189)	< 0.0001	390 (144)	404 (98)	343 (122)	372 (212)	0.03	372 (145)
Men	419 (128)	380 (124)	398 (194)	0.03	396 (143)	493 (156)	321 (158)	296 (138)	0.003	322 (172)
Age < 65 years	406 (127)	326 (102)	280 (81)	< 0.0001	356 (129)	372 (76)	321 (90)	294 (167)	0.03	326 (132)
Age 65-79 years	422 (103)	387 (141)	386 (172)	0.08	396 (136)	435 (148)	335 (140)	312 (132)	0.004	356 (150)
Age ≥ 80 years	448 (121)	394 (120)	454 (136)	0.05	441 (140)	482 (156)	392 (166)	398 (227)	0.22	406 (224)
Diameter of PT (mm) <sup>3</sup>										
Overall	26.0 (4.0)	27.0 (6.0)	27.0 (5.0)	0.002	26.0 (5.0)	27.0 (7.0)	27.5 (5.0)	29.0 (6.0)	0.05	28.0 (6.0)
Women	25.0 (5.0)	26.5 (5.0)	27.0 (4.2)	0.02	26.0 (6.0)	26.0 (6.0)	27.0 (5.0)	28.0 (4.5)	0.24	27.0 (5.8)
Men	26.0 (5.5)	28.0 (5.0)	27.0 (6.0)	0.33	27.0 (5.0)	29.0 (3.0)	29.0 (8.0)	30.0 (4.8)	0.45	29.0 (5.2)
Age < 65 years	25.0 (4.8)	26.0 (6.0)	27.0 (5.0)	0.11	26.0 (5.0)	25.5 (6.2)	25.0 (6.0)	28.0 (7.5)	0.06	26.0 (5.2)
Age 65-79 years	26.0 (5.0)	27.0 (5.0)	27.0 (5.0)	0.24	27.0 (5.0)	28.0 (8.0)	27.0 (4.0)	29.0 (4.8)	0.2	28.0 (6.0)
Age ≥ 80 years	26.0 (4.0)	28.0 (8.5)	28.0 (6.8)	0.04	27.0 (6.0)	29.0 (5.0)	30.5 (5.2)	29.0 (5.0)	0.43	29.0 (5.2)

Note. — Unless otherwise indicated, data are number of examinations and data in parentheses are the interquartile range., HU = hounsfield unit, mm = millimeter, PT = pulmonary trunk, IV = intravenous, ROI= region of interest

<sup>1</sup> Data in parentheses are the percentage.

<sup>2</sup> The measurement was done by calculating the SD of HU within a circular ROI of 1 cm<sup>2</sup> in the descending aorta at the level of the PT.

<sup>3</sup> The diameters of the PT and ascending aorta were measured at the level of the PT.

□ The measurement was done by calculating the mean HU in a circular ROI of 2 cm<sup>2</sup> just proximal to the PT bifurcation.

## Model segmentation performance evaluation on the internal and external testing dataset

Segmentation performance was evaluated for three major blood vessels: the descending aorta (DAo), ascending aorta (AAo), and pulmonary trunk (PT), on an internal test dataset of 210 CTPAs. The trained nnU-Net deep learning model successfully detected all three major blood vessels in all 210 CTPAs. However, there were segmentation failures in 3 cases for the DAo, 8 cases for the AAo, and 15 cases for the PT. For the successfully segmented vessels, the median Dice scores for the DAo were 0.94 (IQR, 0.05) for good quality, 0.95 (IQR, 0.05) for acceptable quality, and 0.95 (IQR, 0.04) for inferior quality examinations. For the AAo, the scores were 0.96 (IQR, 0.04), 0.96 (IQR, 0.05), and 0.95 (IQR, 0.05), respectively. Similarly, for the PT, the scores were 0.96 (IQR, 0.05), 0.95 (IQR, 0.04), and 0.95 (IQR, 0.04), corresponding to good, acceptable, and inferior quality examinations. A combined overall median Dice score of 0.95 (IQR, 0.05) for these three major blood vessels was achieved on the internal test dataset (**Figure 3, A**). AAo segmentation was performed on 12 contrast-enhanced CT examinations from the SegTHOR dataset [21]. The median Dice, Jaccard, and Boundary F1 (BF) contour matching scores were 0.94 (IQR, 0.02), 0.88 (IQR, 0.04), and 1.0, respectively (**Figure 3, B**).

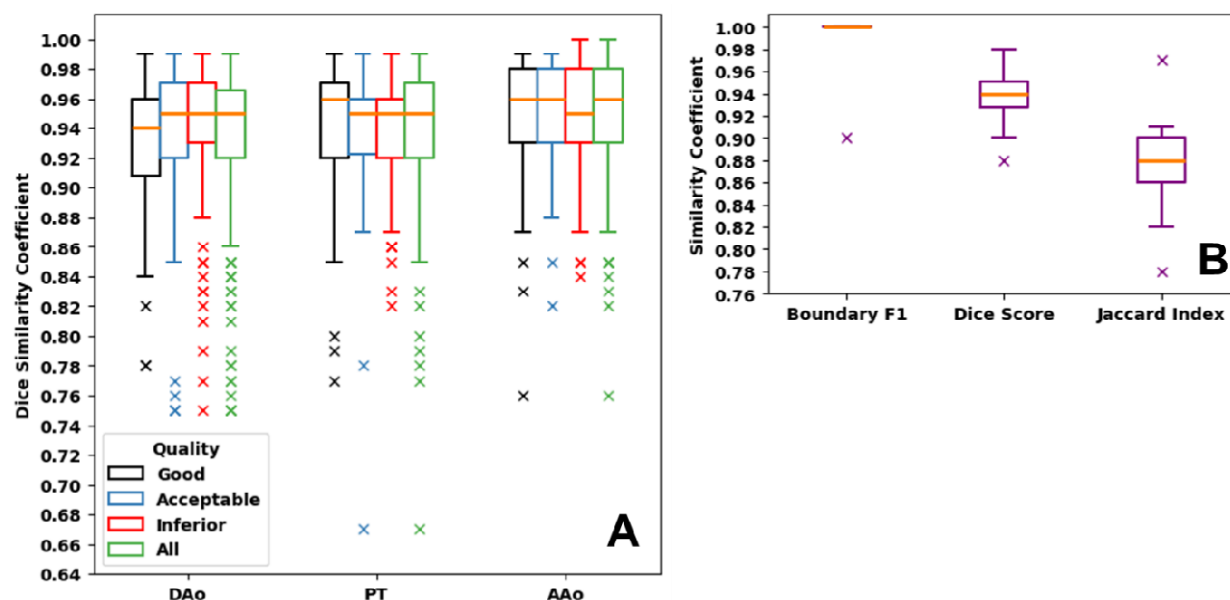


**Figure 3 Segmentation performance on the internal and external test sets.** (A) The internal test set segmentation performance, measured by the Dice Similarity Coefficient (DSC), is provided for all tasks, including the descending aorta (DAo,  $n=207$  CTPA exams), the pulmonary trunk (PT,  $n=195$  CTPA exams), and the ascending aorta (AAo,  $n=202$  CTPA exams). The quality of each CTPA examination was rated by a radiologist as good (black), acceptable (blue), or inferior (red). Green boxes represent the DSC for all quality ratings. (B) The Boundary F1, Dice, and Jaccard index scores for AAo segmentation are provided for the SegTHOR dataset ( $n=12$  CT exams with contrast agent). The median (orange line), interquartile range (boxes), and outliers (x) are shown.

### **Model measurement performance evaluation on the internal and external testing dataset**

Measurement evaluations were conducted on the successfully segmented vessels. Image noise was assessed on 207 CTPAs, the diameter of the AAo on 202 CTPAs, and both the IV contrast concentration in PT and the diameter of the PT on 195 CTPAs from the internal testing dataset. These measurements resulted in Pearson's  $r$  values of 0.91, 0.93, 0.98, and 0.55, respectively, all with  $p < 0.001$  (**Figure 4, A1-D1**). The proposed model's measurements compared favorably with those of the radiologist, with mean differences observed for image noise (-0.03 HU), AAo diameter (1.78 mm), PT IV contrast level (17.62 HU), and PT diameter (-2.16 mm) (**Figure 4, A2-D2**). We also present the mean percentage differences between the proposed model and the radiologist using Bland-Altman analysis: -1.96% for image noise, 5.56% for the AAo diameter, and -7.65% for the PT diameter) (**Figure 4, A3-D2**).

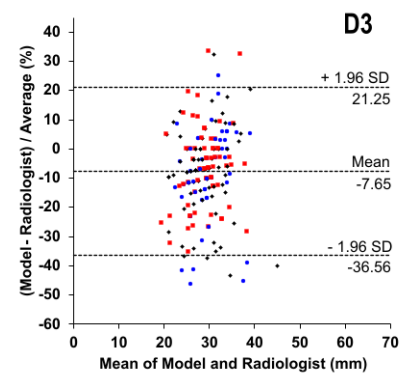
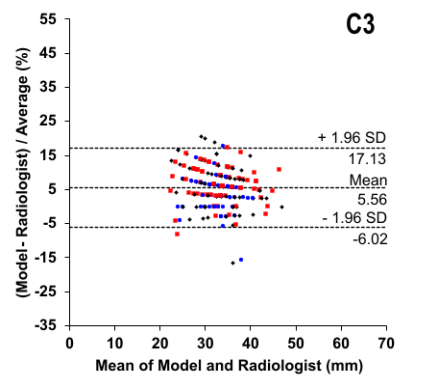
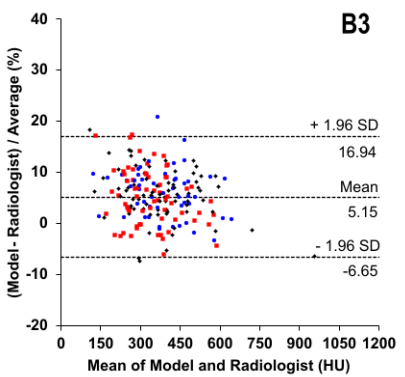
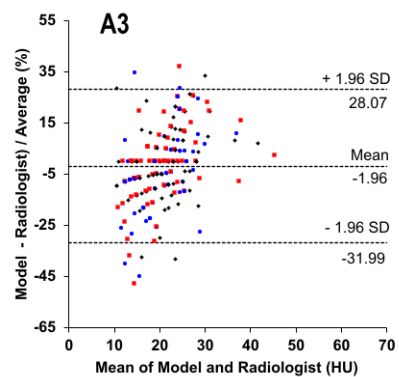
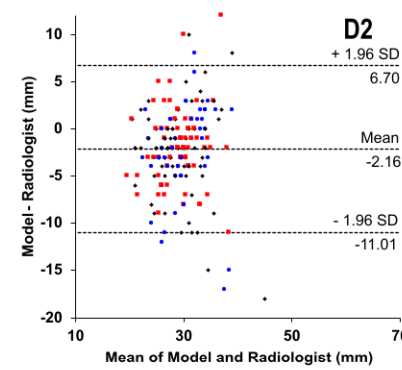
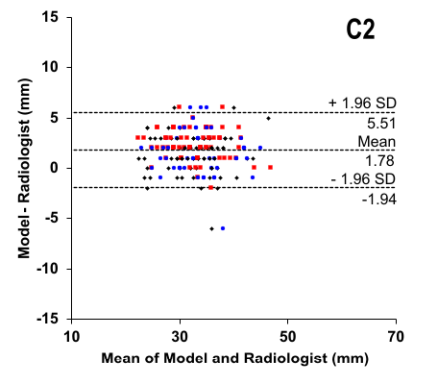
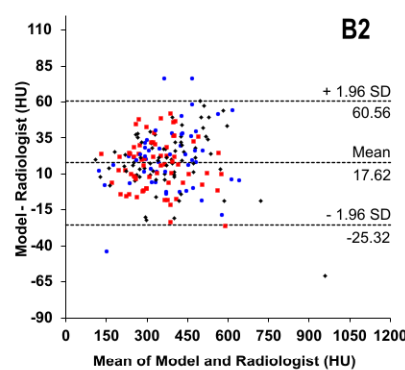
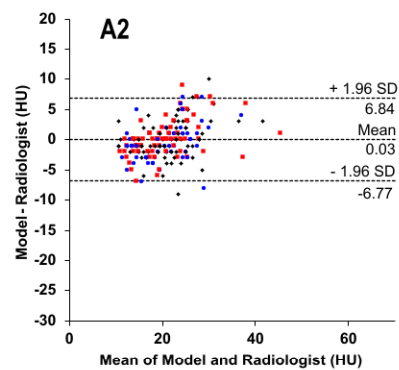
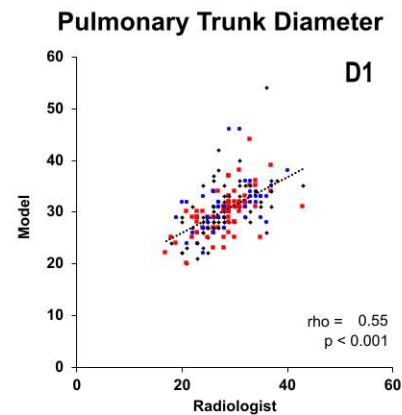
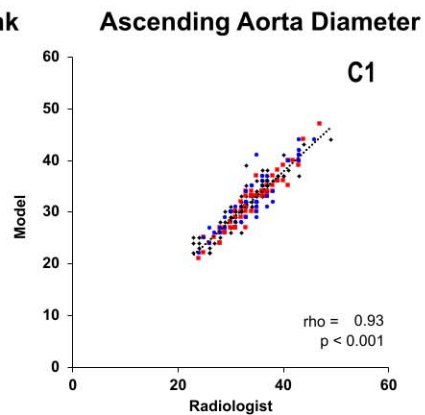
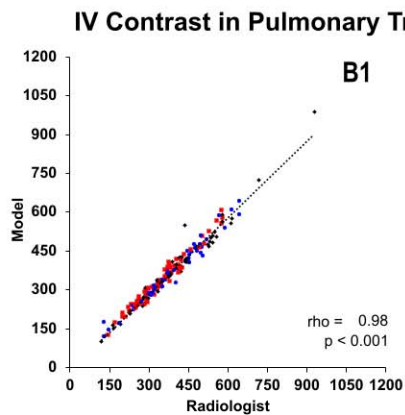
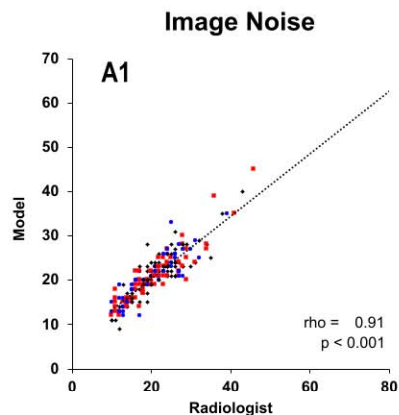


**Figure 4. Comparison of developed AI model to the Radiologist.** Both automatic and manual measurements from the test set cases were evaluated using regression analysis (top row, dashed regression lines), Bland-Altman plots for differences in radiodensity and diameters (middle row, limits of agreement from -1.96 to +1.96 SD), and Bland-Altman plots for percentage differences (bottom row, limits of agreement from -1.96 to +1.96 SD). The analysis included: (A) Image noise (n=207 CTPA exams), (B) Intravenous (IV) contrast agent in pulmonary trunk (n=195 CTPA exams), (C) Ascending aorta diameter (n=202 CTPA exams), and (D) Pulmonary trunk diameter (n=195 CTPA exams). The quality of each CTPA examination was rated by the radiologist as good (black diamonds), acceptable (blue circles), or inferior (red squares).

For the external evaluation of measurements, PT diameter was assessed in 35 CTPA exams from the FUMPE dataset. First, inference was performed using a trained nnU-Net DL model, followed by the selection of the best 2D PT segmentation candidate through a post-processing algorithm. Finally, a measurement algorithm was applied, resulting in Pearson's  $r = 0.83$ ,  $p < 0.001$  (**Figure 5, A**). The limits of agreement between the proposed model and FUMPE radiologist annotations showed mean differences of -1.43 mm and -5.14% (**Figure 5, B and C**).

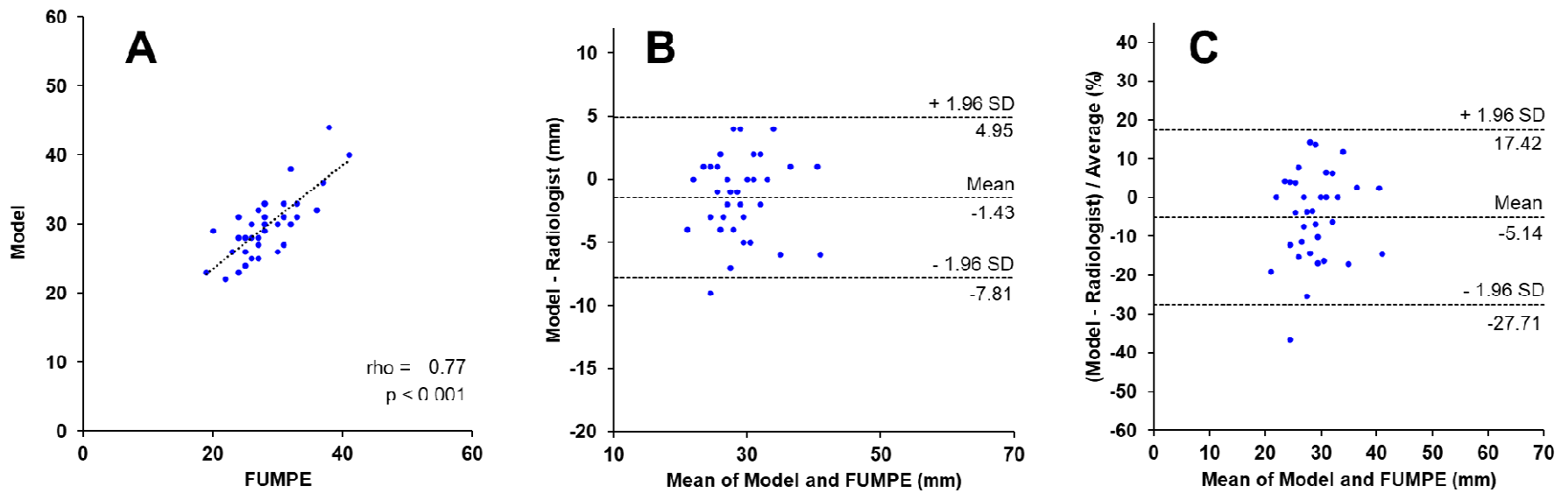


**Figure 5. External Testing of Automatic Pulmonary Trunk (PT) Diameter Measurement.** Automatic PT diameter measurements from the FUMPE dataset (35 CTPA exams) were compared to manual radiologist annotations from the original study using three methods: (A) regression analysis, depicted with dashed regression lines, (B) Bland-Altman plots of differences in millimeters, with limits of agreement from -1.96 to +1.96 SD, and (C) Bland-Altman plots of percentage differences, with the same limits of agreement.



## Segmentation and measurement performance comparison with the previous solution

This study demonstrates significant improvements in segmentation performance over our previously proposed fully automated deterministic solution [19], particularly with higher success rates for segmenting the DAo (99% vs. 90%), AAO (96% vs. 86%), and PT (93% vs. 88%) in the internal test set. Measurement performance had notable improvements in image noise (0.03 HU vs. -0.25 HU) and the diameter of the PT (-2.16 mm vs. -3.20 mm), but a larger variance in the diameter of the AAO (1.78 mm vs. 0.51 mm) and IV contrast concentration in the PT (17.62 HU vs. -0.28 HU) (**Table 3**). Overall, the current study provides enhanced segmentation accuracy, while measurement accuracy improvements are more variable.

*Table 3 Comparison of Segmentation and Measurement Performance Between the Current and Previous Solution*

Characteristics	Previous Solution	This Study
<b>Segmentation Performance</b>		
Internal test set	520 CTPAs	210 CTPAs
DAo	470 (90)	207 (99)
AAo	447 (86)	202 (96)
PT	455 (88)	195 (93)
External set	12 CTPAs	
AAo	12 (100)	12 (100)
<b>Measurement Performance (mean differences) <sup>1</sup></b>		
Internal test set		
Image noise (HU)	-0.25	0.03
Diameter of ascending aorta (mm)	0.51	1.78
IV contrast concentration in PT (HU)	-0.28	17.62
Diameter of PT (mm)	-3.20	-2.16
External set	31 CTPAs	35 CTPAs
Diameter of PT (mm)	-2.6	-1.43

Note. — Unless otherwise indicated, data are presented as the number of examinations, with percentages shown in parentheses. HU = Hounsfield unit, mm = millimeter, PT = pulmonary trunk, IV = intravenous, CTPA = computed tomography pulmonary angiography

<sup>1</sup> The measurements were performed only on successfully segmented vessels.

## Discussion

In this study, a nnU-Net [18] based deep learning (DL) model was used along with a deterministic post-processing step to automatically segment major blood vessels including descending aorta (DAo), ascending aorta (AAo), and pulmonary trunk (PT). The proposed model achieved robust segmentation of major blood vessels, with a combined overall median Dice score of 0.95 (interquartile range, 0.05). For successfully segmented vessels, a 2D measurement algorithm [19] was adapted and subsequently applied to achieve accurate vessel measurements. The automatic measurements showed a strong correlation with the radiologist's assessments, with Pearson correlation coefficients ranging from 0.55 to 0.98.

The comparison of segmentation methods for vascular structures, including traditional image processing approaches such as multi-atlas segmentation and model-based frameworks as well as modern artificial intelligence methods like deep learning models, revealed varying performance across different techniques. Our proposed method significantly outperformed our previous fully automated deterministic solution [19], particularly in segmenting the DAo, AAo, and PT. Segmentation success rates increased by 9%, 10%, and 5%, respectively, on the internal test set. Zhuang et al. employed multi-atlas segmentation on 30 cases, achieving high dice score for the AAo (0.96) but lower performance for the pulmonary trunk (0.79), highlighting the challenge of segmenting complex structures. In contrast, Ecabert et al. used a model-based framework with geometric mesh modeling and deformable models on 37 cases, delivering strong and consistent scores for both the aorta (0.95) and PT (0.94), indicating the robustness of their method in 3D segmentation tasks. Deep learning approaches, particularly U-Net-based semantic segmentation architectures, have demonstrated outstanding performance in numerous studies [15,25–27]. Baskaran et al. [15] tested their U-Net model on 20 cases, achieving high Dice scores for the aorta (0.97 for the ascending and 0.95 for the descending sections), but a lower score for the pulmonary trunk (0.78). Sharkey et al. [25] utilized nnU-Net, tested on internal test set of 100 cases, showing stable results across vessels, with scores of 0.92 for the AAo, 0.91 for the DAo, and 0.93 for the PT. They also evaluated an external test set of 20 cases, where performance remained similar, except for a slightly lower score in the DAo (0.87). Román et al. [26] proposed a new architecture similar to V-Net for PT segmentation, achieving a Dice score of 0.89 on a test

set of 91 cases. In summary, U-Net-based deep learning architectures outperform other methods in vascular segmentation but struggle with complex vascular structures like the pulmonary trunk.

Compared to U-Net-based semantic segmentation architectures, AI foundation models like the Segment Anything Model (SAM) have demonstrated improved generalization, efficiency, performance, and accessibility [28]. SAM, developed by Meta AI Research [29], was trained on the largest image segmentation dataset to date, comprising over 1 billion masks across 11 million images. Ma et al. introduced MedSAM, a refined version of SAM specifically designed for medical image segmentation. However, despite these advancements, MedSAM and nnU-Net models achieved similar Dice scores of 0.94 and 0.93 for aorta segmentation [30]. In contrast, our model, tested on a larger dataset of 210 cases, performed consistently well with accuracy rates of 0.95–0.96 across both the aorta and PT, demonstrating competitive results despite utilizing 2D image segmentation and accounting for variable examinations quality. A deterministic algorithm was developed to select the optimal 2D object of the major blood vessels from the candidate pool for measurement. However, this algorithm failed in 3, 8, and 15 cases for the DAo, AAo, and PT, respectively. The primary reason for these failures was inferior or acceptable examination quality of the cases. When our proposed segmentation method was evaluated on a publicly available dataset, it demonstrated comparable performance on both internal and external datasets, achieving a median Dice score of 0.95 (IQR, 0.05) for the AAo on the internal testing dataset and 0.94 (IQR, 0.02) on the external SegThor dataset [21]. Collectively, our method delivers robust and consistent segmentation performance while addressing the limitations of variability in CTPA examination quality and dataset generalization.

Our study provides valuable insights into the measurement of major blood vessels, though it is limited by the constraints of 2D segmentation and measurement. While the majority of the literature focuses on 3D segmentation of the aorta and PT, our 2D approach offers a more efficient and task-specific method for segmenting the DAo, AAo, and PT. This approach provides several practical advantages, including the requirement for only 2D manual annotations for model development, reduced computational power, and lower algorithmic complexity. We observed comparable measurement performance compared to previous studies. On a test dataset of 288 contrast-enhanced chest CT scans, Chettrit et al. reported mean differences between their

algorithm and radiologists of -0.94 mm for the AAo diameter and -0.86 mm for the PT diameter [31]. Román et al. [26] measured the mean error of the PT radius by calculating the average Euclidean distance between the segmented surface and the ground truth surface using the Discrete Marching Cubes method, resulting in an error of 1.25 mm. In a prior study, we reported mean differences of -3.20 mm for the PT diameter and 0.51 mm for the AAo diameter between their automated measurements and ground truth [19]. Here, we observed larger discrepancies for the AAo, with a mean difference of 1.78 mm between automated measurements and those of radiologists. However, for the PT diameter, the mean absolute difference between the model's measurements and those of radiologists was -2.16 mm on our internal dataset, which improved to -1.43 mm on the external FUMPE dataset [22].

There are several limitations to our study. First, the model was initially trained on data collected from a single institution, albeit produced using scanners from a variety of vendors. Second, supplementary structural features, including the right-to-left ventricular diameter ratio [32], contrast reflux into the inferior vena cava [33], and cardiac chamber dimensions [34], can provide valuable prognostic or diagnostic information beyond the diameter of the AAo and PT. Third, due to the unavailability of a publicly accessible dataset, we could not evaluate our proposed model on a large external testing set. Fourth, to validate the generalizability of the proposed model, it should be evaluated on various CT protocols, including coronary CT angiography and venous phase contrast-enhanced CT, in addition to CTPA. Finally, while the proposed method achieved better segmentation results compared to our previous solution, we observed significant variability in IV contrast concentration in the PT and in the diameter of the AAo. This discrepancy is primarily due to the measurement algorithm, which was adapted from our solution but was originally designed for that specific segmentation algorithm. Therefore, to improve accuracy in future studies, a new measurement algorithm needs to be developed specifically for our current segmentation method.

In conclusion, the automated end-to-end deep learning-based segmentation model accurately segmented major blood vessels in the chest cavity, and the adapted vessel measurement algorithm showed strong correlation with radiologists' measurements. Integrating the highly

accurate automated solutions presented in this study into Picture Archiving and Communication Systems (PACS) could be of value for radiologists in routine clinical practice.

**Data sharing statement:** Data generated or analyzed during the study are available from the corresponding author upon reasonable request.

### **Funding information**

The project was supported by a grant from Analytic Imaging Diagnostics Arena (AIDA), <https://medtech4health.se/aida-en/>, to Tobias Sjöblom. Tomas Fröding and Dimitrios Toumpanakis were supported by clinical fellowships from AIDA. Tomas Fröding was supported by the Centre for Clinical Research Sörmland, Uppsala University, Eskilstuna, Sweden.

**Acknowledgements.** The project was supported by a grant from Analytic Imaging Diagnostics Arena (AIDA) to Tobias Sjöblom. Tomas Fröding and Dimitrios Toumpanakis were financially supported by clinical fellowships from AIDA. Tomas Fröding was financially supported by the Centre for Clinical Research Sörmland, Uppsala University.

## References

1. Li Y, Cao G, Jing W, Liu J, Liu M. Global trends and regional differences in incidence and mortality of cardiovascular disease, 1990–2019: findings from 2019 global burden of disease study. *Eur J Prev Cardiol.* 2023;30: 276–286. doi:10.1093/eurjpc/zwac285
2. Kolossváry M, Kellermayer M, Merkely B, Maurovich-Horvat P. Cardiac Computed Tomography Radiomics: A Comprehensive Review on Radiomic Techniques. *J Thorac Imaging.* 2018;33: 26–34. doi:10.1097/RTI.0000000000000268
3. Fusco R, Granata V, Grazzini G, Pradella S, Borgheresi A, Bruno A, et al. Radiomics in medical imaging: pitfalls and challenges in clinical management. *Jpn J Radiol.* 2022;40: 919–929. doi:10.1007/s11604-022-01271-4
4. Baeßler B, Engelhardt S, Hekalo A, Hennemuth A, Hüllebrand M, Laube A, et al. Perfect Match: Radiomics and Artificial Intelligence in Cardiac Imaging. *Circ Cardiovasc Imaging.* 2024;17. doi:10.1161/CIRCIMAGING.123.015490
5. Konstantinides SV, Meyer G, Becattini C, Bueno H, Geersing G-J, Aujesky D, et al. 2019 ESC Guidelines for the diagnosis and management of acute pulmonary embolism developed in collaboration with the European Respiratory Society (ERS). *Eur Heart J.* 2020;41: 543–603. doi:10.1093/eurheartj/ehz405
6. Schönfeld T, Seitz P, Kriehoff C, Ponorac S, Wötzel A, Olthoff S, et al. High-pitch CT pulmonary angiography (CTPA) with ultra-low contrast medium volume for the detection of pulmonary embolism: a comparison with standard CTPA. *Eur Radiol.* 2023;34: 1921–1931. doi:10.1007/s00330-023-10101-8
7. Hrdlicka J, Jurka M, Bircakova B, Ambroz D, Jansa P, Burgetova A, et al. Even non-expert radiologists report chronic thromboembolic pulmonary hypertension (CTEPH) on CT pulmonary angiography with high sensitivity and almost perfect agreement. *Eur Radiol.* 2023;34: 1086–1093. doi:10.1007/s00330-023-10098-0
8. Xu W, Deng M, Xi L, Liu A, Yang H, Tao X, et al. Comparison of cardiovascular metrics on computed tomography pulmonary angiography of the updated and old diagnostic criteria for pulmonary hypertension in patients with chronic thromboembolic pulmonary hypertension. *Quant Imaging Med Surg.* 2023;13: 7910–7923. doi:10.21037/qims-23-250
9. Scarpato BM, Locke BW, Bledsoe J, Knox DB, Conner K, Stoddard GJ, et al. The association between pulmonary artery enlargement and mortality in an Emergency Department population undergoing computed tomography pulmonary angiography. *Pulm Circ.* 2023;13: e12225. doi:10.1002/pul2.12225
10. Zhao W, Guo J, Dong N, Hei H, Duan X, Shen C. Diagnostic value of 3D volume measurement of central pulmonary artery based on CTPA images in the pulmonary hypertension. *BMC Med Imaging.* 2023;23: 211. doi:10.1186/s12880-023-01180-6

11. Pienn M, Gertz RJ, Gerhardt F, Kröger JR, Zaytoun H, Reimer RP, et al. CT-derived lung vessel morphology correlates with prognostic markers in precapillary pulmonary hypertension. *J Heart Lung Transplant*. 2024;43: 54–65. doi:10.1016/j.healun.2023.08.013
12. Ecabert O, Peters J, Walker MJ, Ivanc T, Lorenz C, Von Berg J, et al. Segmentation of the heart and great vessels in CT images using a model-based adaptation framework. *Med Image Anal*. 2011;15: 863–876. doi:10.1016/j.media.2011.06.004
13. Moses D, Sammut C, Zrimec T. Automatic segmentation and analysis of the main pulmonary artery on standard post-contrast CT studies using iterative erosion and dilation. *Int J Comput Assist Radiol Surg*. 2016;11: 381–395. doi:10.1007/s11548-015-1265-3
14. Zhuang X, Bai W, Song J, Zhan S, Qian X, Shi W, et al. Multiatlas whole heart segmentation of CT data using conditional entropy for atlas ranking and selection. *Med Phys*. 2015;42: 3822–3833. doi:10.1118/1.4921366
15. Baskaran L, Al’Aref SJ, Maliakal G, Lee BC, Xu Z, Choi JW, et al. Automatic segmentation of multiple cardiovascular structures from cardiac computed tomography angiography images using deep learning. Zirlik A, editor. *PLOS ONE*. 2020;15: e0232573. doi:10.1371/journal.pone.0232573
16. Suzuki H, Kawata Y, Aokage K, Matsumoto Y, Sugiura T, Tanabe N, et al. Aorta and main pulmonary artery segmentation using stacked U-Net and localization on non-contrast-enhanced computed tomography images. *Med Phys*. 2024;51: 1232–1243. doi:10.1002/mp.16654
17. Koo HJ, Lee J-G, Lee J-B, Kang J-W, Yang DH. Deep Learning Based Automatic Segmentation of the Thoracic Aorta from Chest Computed Tomography in Healthy Korean Adults. *Eur J Vasc Endovasc Surg*. 2024; S1078588424006427. doi:10.1016/j.ejvs.2024.07.030
18. Isensee F, Jaeger PF, Kohl SAA, Petersen J, Maier-Hein KH. nnU-Net: a self-configuring method for deep learning-based biomedical image segmentation. *Nat Methods*. 2021;18: 203–211. doi:10.1038/s41592-020-01008-z
19. Kahraman AT, Fröding T, Toumpanakis D, Sladoje N, Sjöblom T. Automated detection, segmentation and measurement of major vessels and the trachea in CT pulmonary angiography. *Sci Rep*. 2023;13: 18407. doi:10.1038/s41598-023-45509-1
20. Wolf I, Vetter M, Wegner I, Böttger T, Nolden M, Schöbinger M, et al. The Medical Imaging Interaction Toolkit. *Med Image Anal*. 2005;9: 594–604. doi:10.1016/j.media.2005.04.005
21. Lambert Z, Petitjean C, Dubray B, Kuan S. SegTHOR: Segmentation of Thoracic Organs at Risk in CT images. 2020 Tenth International Conference on Image Processing Theory, Tools and Applications (IPTA). Paris, France: IEEE; 2020. pp. 1–6. doi:10.1109/IPTA50016.2020.9286453



22. Masoudi M, Pourreza H-R, Saadatmand-Tarzjan M, Eftekhari N, Zargar FS, Rad MP. A new dataset of computed-tomography angiography images for computer-aided detection of pulmonary embolism. *Sci Data*. 2018;5: 180180. doi:10.1038/sdata.2018.180
23. Csurka G, Larlus D, Perronnin F, Meylan F. What is a good evaluation measure for semantic segmentation?. *Bmvc*. Bristol; 2013. pp. 10–5244. Available: <https://projet.liris.cnrs.fr/imagine/pub/proceedings/BMVC-2013/Papers/paper0033/paper0033.pdf>
24. Bland JM, Altman D. Statistical methods for assessing agreement between two methods of clinical measurement. *The lancet*. 1986;327: 307–310. doi:10.1016/S0140-6736(86)90837-8
25. Sharkey MJ, Taylor JC, Alabed S, Dwivedi K, Karunasaagarar K, Johns CS, et al. Fully automatic cardiac four chamber and great vessel segmentation on CT pulmonary angiography using deep learning. *Front Cardiovasc Med*. 2022;9: 983859. doi:10.3389/fcvm.2022.983859
26. López-Linares Román K, De La Bruere I, Onieva J, Andresen L, Qvortrup Holsting J, Rahaghi FN, et al. 3D Pulmonary Artery Segmentation from CTA Scans Using Deep Learning with Realistic Data Augmentation. In: Stoyanov D, Taylor Z, Kainz B, Maicas G, Beichel RR, Martel A, et al., editors. *Image Analysis for Moving Organ, Breast, and Thoracic Images*. Cham: Springer International Publishing; 2018. pp. 225–237. doi:10.1007/978-3-030-00946-5\_23
27. Wasserthal J, Breit H-C, Meyer MT, Pradella M, Hinck D, Sauter AW, et al. TotalSegmentator: Robust Segmentation of 104 Anatomic Structures in CT Images. *Radiol Artif Intell*. 2023;5: e230024. doi:10.1148/ryai.230024
28. Schneider J, Meske C, Kuss P. Foundation Models: A New Paradigm for Artificial Intelligence. *Bus Inf Syst Eng*. 2024;66: 221–231. doi:10.1007/s12599-024-00851-0
29. Kirillov A, Mintun E, Ravi N, Mao H, Rolland C, Gustafson L, et al. Segment Anything. *arXiv*; 2023. doi:10.48550/ARXIV.2304.02643
30. Ma J, He Y, Li F, Han L, You C, Wang B. Segment anything in medical images. *Nat Commun*. 2024;15: 654. doi:10.1038/s41467-024-44824-z
31. Chettrit D, Bregman Amitai O, Tamir IA, Bar A, Elnekave E. PHT-bot: a deep learning based system for automatic risk stratification of COPD patients based upon signs of pulmonary hypertension. In: Hahn HK, Mori K, editors. *Medical Imaging 2019: Computer-Aided Diagnosis*. San Diego, United States: SPIE; 2019. p. 23. doi:10.1117/12.2512469
32. Ghani H, Weir-McCall JR, Ruggiero A, Pepke-Zaba J. Imaging in chronic thromboembolic pulmonary disease: Current practice and advances. *Int J Cardiol Congenit Heart Dis*. 2024;17: 100536. doi:10.1016/j.ijcchd.2024.100536

33. Zantonelli G, Cozzi D, Bindi A, Cavigli E, Moroni C, Luvarà S, et al. Acute Pulmonary Embolism: Prognostic Role of Computed Tomography Pulmonary Angiography (CTPA). *Tomography*. 2022;8: 529–539. doi:10.3390/tomography8010042
34. Melzig C, Do TD, Egenlauf B, Partovi S, Grünig E, Kauczor H-U, et al. Diagnostic accuracy of automated 3D volumetry of cardiac chambers by CT pulmonary angiography for identification of pulmonary hypertension due to left heart disease. *Eur Radiol*. 2022;32: 5222–5232. doi:10.1007/s00330-022-08663-0

**Supplementary Table 1. Ground Truth Measurements by Radiologists.**

Category	Training Dataset						Test Dataset					
	Quality of CTPA exams				Overall	p-value	Quality of CTPA exams				Overall	p-value
	Good	Acceptable	Inferior	p-value			Good	Acceptable	Inferior	p-value		
<b>No. of CTPA exams <sup>1</sup></b>												
Women	121 (24.69)	80 (16.33)	56 (11.43)		257 (52.45)		41 (19.52)	41 (19.52)	44 (20.95)		126 (59.99)	
Men	79 (16.12)	78 (15.92)	76 (15.51)		233 (47.55)		17 (8.1)	29 (13.81)	38 (18.1)		84 (40.01)	
Age < 65 years	62 (12.65)	50 (10.2)	33 (6.73)	-	145 (29.58)	-	16 (7.62)	21 (10)	23 (10.95)	-	60 (28.57)	-
Age 65-79 years	92 (18.78)	78 (15.92)	61 (12.45)		231 (47.15)		25 (11.9)	31 (14.76)	30 (14.29)		86 (40.95)	
Age ≥ 80 years	46 (9.39)	30 (6.12)	38 (7.76)		114 (23.27)		17 (8.1)	18 (8.57)	29 (13.81)		64 (30.48)	
<b>Image noise (HU) <sup>2</sup></b>												
Overall	19.0 (9.0)	20.0 (7.0)	23.0 (7.0)	< 0.0001	20.5 (8.0)	-	16.0 (9.8)	20.0 (8.8)	23.5 (8.0)	< 0.0001	20.0 (10.0)	-
Women	19.0 (10.0)	20.5 (7.0)	21.0 (8.0)	0.02	20.0 (9.0)		16.0 (9.0)	20.0 (7.0)	23.0 (8.0)	0.0004	20.0 (10.0)	
Men	20.0 (7.0)	20.0 (7.0)	23.5 (5.2)	0.0002	21.0 (8.0)	0.09	16.0 (9.0)	19.0 (10.0)	24.0 (8.8)	0.003	21.0 (9.5)	0.34
Age < 65 years	21.0 (8.0)	19.0 (7.8)	21.0 (8.0)	0.92	20.0 (8.0)		15.5 (12.2)	18.0 (8.0)	22.0 (6.5)	0.11	20.0 (9.5)	
Age 65-79 years	18.5 (9.2)	20.5 (7.8)	23.0 (6.0)	0.0001	20.0 (9.0)	0.41	18.0 (7.0)	20.0 (8.0)	24.0 (7.8)	0.006	20.0 (8.8)	0.62
Age ≥ 80 years	19.0 (9.8)	20.5 (6.5)	23.5 (4.8)	0.001	21.0 (7.8)		14.0 (5.0)	21.0 (9.5)	24.0 (9.0)	0.0005	20.0 (10.8)	
<b>Diameter of ascending aorta (mm) <sup>3</sup></b>												
Overall	32.0 (6.0)	33.0 (5.0)	34.0 (6.0)	0.01	33.0 (6.0)	-	35.0 (6.5)	33.0 (6.0)	34.0 (6.0)	0.07	34.0 (6.0)	-
Women	31.0 (5.0)	32.0 (5.0)	32.0 (7.0)	0.45	31.0 (6.0)		34.0 (6.0)	31.0 (7.0)	32.0 (4.0)	0.11	33.0 (6.5)	
Men	34.0 (6.0)	35.0 (4.8)	35.0 (5.2)	0.22	35.0 (5.0)	< 0.0001	38.0 (7.0)	35.0 (4.0)	36.0 (4.8)	0.07	36.0 (5.0)	< 0.0001
Age < 65 years	29.5 (6.0)	31.0 (5.8)	31.0 (8.0)	0.3	31.0 (7.0)		32.0 (7.8)	29.0 (6.0)	31.0 (5.0)	0.39	31.0 (7.0)	
Age 65-79 years	34.0 (5.2)	34.0 (4.0)	34.0 (4.0)	0.72	34.0 (5.0)	< 0.0001	35.0 (7.0)	33.0 (6.5)	35.0 (4.0)	0.28	35.0 (6.0)	< 0.0001
Age ≥ 80 years	33.0 (6.0)	35.0 (5.8)	36.0 (5.8)	0.01	35.0 (7.0)		37.0 (3.0)	35.5 (3.5)	36.0 (6.0)	0.34	36.0 (5.0)	
<b>IV contrast concentration in PT (HU) <sup>□</sup></b>												
Overall	425 (125)	370 (134)	374 (193)	< 0.0001	394 (146)	-	406 (141)	334 (148)	316 (167)	< 0.0001	358 (158)	-
Women	432 (123)	363 (135)	351 (189)	< 0.0001	390 (144)		404 (98)	343 (122)	372 (212)	0.03	372 (145)	
Men	419 (128)	380 (124)	398 (194)	0.03	396 (143)	0.97	493 (156)	321 (158)	296 (138)	0.003	322 (172)	0.16
Age < 65 years	406 (127)	326 (102)	280 (81)	< 0.0001	356 (129)		372 (76)	321 (90)	294 (167)	0.03	326 (132)	
Age 65-79 years	422 (103)	387 (141)	386 (172)	0.08	396 (136)	< 0.0001	435 (148)	335 (140)	312 (132)	0.004	356 (150)	0.002
Age ≥ 80 years	448 (121)	394 (120)	454 (136)	0.05	441 (140)		482 (156)	392 (166)	398 (227)	0.22	406 (224)	
<b>Diameter of PT (mm) <sup>3</sup></b>												
Overall	26.0 (4.0)	27.0 (6.0)	27.0 (5.0)	0.002	26.0 (5.0)	-	27.0 (7.0)	27.5 (5.0)	29.0 (6.0)	0.05	28.0 (6.0)	-
Women	25.0 (5.0)	26.5 (5.0)	27.0 (4.2)	0.02	26.0 (6.0)		26.0 (6.0)	27.0 (5.0)	28.0 (4.5)	0.24	27.0 (5.8)	
Men	26.0 (5.5)	28.0 (5.0)	27.0 (6.0)	0.33	27.0 (5.0)	0.001	29.0 (3.0)	29.0 (8.0)	30.0 (4.8)	0.45	29.0 (5.2)	0.001
Age < 65 years	25.0 (4.8)	26.0 (6.0)	27.0 (5.0)	0.11	26.0 (5.0)		25.5 (6.2)	25.0 (6.0)	28.0 (7.5)	0.06	26.0 (5.2)	
Age 65-79 years	26.0 (5.0)	27.0 (5.0)	27.0 (5.0)	0.24	27.0 (5.0)	0.03	28.0 (8.0)	27.0 (4.0)	29.0 (4.8)	0.2	28.0 (6.0)	0.001
Age ≥ 80 years	26.0 (4.0)	28.0 (8.5)	28.0 (6.8)	0.04	27.0 (6.0)		29.0 (5.0)	30.5 (5.2)	29.0 (5.0)	0.43	29.0 (5.2)	

Note. — Unless otherwise indicated, data are number of examinations and data in parentheses are the interquartile range., HU = hounsfield unit, mm = millimeter, PT = pulmonary trunk, IV = intravenous, ROI=region of interest

<sup>1</sup> Data in parentheses are the percentage.

<sup>2</sup> The measurement was done by calculating the SD of HU within a circular ROI of 1 cm<sup>2</sup> in the descending aorta at the level of the PT.

<sup>3</sup> The diameters of the PT and ascending aorta were measured at the level of the PT.

□ The measurement was done by calculating the mean HU in a circular ROI of 2 cm<sup>2</sup> just proximal to the PT bifurcation.